INORGANIC CHEMISTRY
FRONTIERS

RESEARCH ARTICLE

View Article Online
View Journal | View Issue

Cite this: *Inorg. Chem. Front.*, 2017, **4**, 1231

MOF-templated nitrogen-doped porous carbon materials as efficient electrocatalysts for oxygen reduction reactions†

Suhong Wang,‡[a] Lin Liu,‡[a] Shi-Ming Wang *[b] and Zhengbo Han*[a]

Received 28th April 2017,
Accepted 24th May 2017

DOI: 10.1039/c7qi00233e

rsc.li/frontiers-inorganic

MOF-templated nitrogen-doped porous carbon materials (NPCs) have been prepared by employing the previously reported MOF, $[(CH_3)_2NH_2]_6[Ni(H_2O)_6]_3\{Ni_6(\eta^6\text{-TATAT})_4(H_2O)_{12}\}$, as a precursor, which can act as efficient electrocatalysts for oxygen reduction reactions (ORRs). The carbonized MOF acts as the carbon source, and urea is employed as an additional nitrogen source. The urea modified carbon materials, carbonized at 800 °C, 900 °C and 1000 °C under Ar atmosphere, all show electrocatalytic activity for ORRs; the material carbonized at 900 °C exhibits a more appropriate nitrogen content, robust pore structure and an excellent degree of graphitization. In alkaline media, NPC-900 exhibits superior catalytic activity (the onset and half-wave potentials are −0.06 V and −0.23 V *vs.* Ag/AgCl, respectively), excellent long-term durability and outstanding methanol tolerance compared with the commercial Pt/C catalyst.

Introduction

In recent years, fuel cells (FCs) have aroused great interest due to their ability to efficiently convert chemical energy into electricity and their superior durability compared to electrochemical cells. Most importantly, FC products do not pollute the environment, and the wide use of FCs is regarded as one of the most effective solutions to the ever-increasing demand for environmentally friendly high power energy sources.[1] However, the kinetics of oxygen reduction reactions (ORRs) at the cathode is sluggish, which has blocked the development of fuel cells. To date, platinum (Pt) and Pt-based catalysts have been developed and are regarded as the most effective electrocatalysts for ORRs.[2–4] However, Pt-based ORR catalysts still suffer from problems, such as limited stability, fuel crossover and the CO poison effect.[5] At the same time, the noble Pt metal is scarce and is expensive, which is a main obstacle for the commercialization of FCs. Based on the abovementioned aspects, researchers have devoted themselves to finding non-precious metals or metal-free ORR catalysts to replace Pt-based catalysts and reduce the usage of Pt, by avoiding[6,7] Pt-based alloys,[8–10] inorganic hybrid materials,[11,12] transition metal compound-based catalysts, *etc.*[13–16] The carbon materials outshine other materials due to their superior conductive activity, corrosion resistance and surface properties as well as their low cost.[17] Generally, researchers prefer to dope heteroatoms (B,[18,19] N,[20–23] P,[24–26] S[27–29]) into carbon materials to enhance their catalytic activity; nitrogen-doped carbon materials are the most promising metal-free ORR catalysts. Nitrogen-doped carbon nanostructures and their corresponding composites,[30] metal-free N-doped carbon materials (such as graphene-based catalysts,[21,22,31,32] carbon nanotube based catalysts,[33] and porous organic framework-templated nitrogen porous carbons[34]) are all reported as high efficiency ORR catalysts. The ORR catalytic activity of nitrogen-doped carbons strongly depends on the type of nitrogen precursors, the nitrogen content, the heat treatment temperature and so on.

Metal–organic frameworks (MOFs) are periodically arranged by organic linkers and metal ions in three-dimensional space; they are emerging as a new class of crystalline porous materials with large surface area, uniform pore size, higher porosity, and more diverse structures and functions. Recently, MOFs have been utilized as templates or precursors to synthesize nitrogen-doped porous carbon materials,[35] which have attracted researchers' attention due to the large number of available MOFs with versatile pore structures and high carbon content. Nitrogen-doped porous carbon materials exhibit a wide range of energy-related applications in hydrogen storage,

[a]*College of Chemistry, Liaoning University, Shenyang 110036, People's Republic of China. E-mail: ceshzb@lnu.edu.cn*
[b]*College of Light Industry, Liaoning University, Shenyang 110036, People's Republic of China. E-mail: wangsm383@163.com*

†Electronic supplementary information (ESI) available: The PXRD profiles of the MOF in this paper and the XPS spectrum, nitrogen adsorption–desorption isotherm, images SEM, TEM and electrochemical data of NPC-800 and NPC-1000. See DOI: 10.1039/c7qi00233e

‡The two authors contributed equally to this paper.

supercapacitors, lithium–sulfur batteries, and FCs, *etc*.[36–38] As a precursor to the preparation of the carbon-based ORR catalyst, the C-rich ligand is the direct C source, which does not need a second carbon source; the N-containing ligand could be the ideal precursor for preparing the N-doped carbon material. Most importantly, its porous nature made it possible to obtain the porous carbon structure. The porous structure is not only beneficial for high ORR activity, but also facilitates expedient post modification. Currently, some research groups have acquired some porous carbons using MOFs as a template, such as MOF-5, which was employed as a precursor with high surface area and carbon content. Furthermore, post modification of MOF-5 derived carbon *via* g-C_3N_4 entrapment for a metal-free ORR electrocatalyst is also facile.[39] ZIF series are also ideal precursors to prepare nitrogen-doped porous carbons.[40] For example, ZIF-7 and ZIF-8 contain a rich nitrogen source in imidazole ligands, and the carbon materials directly derived from them without an extra N source also show outstanding ORR catalytic activity.[41,42] Some groups have reported the combination of MOFs with graphene oxide;[43] graphene has excellent electrical conductivity and large surface area as well as chemical and mechanical stability, which increases stability and improves electrocatalytic activity in ORR reactions.[44,45] However, there are still specific challenges in large-scale production and in application to fuel cells. Therefore, it is necessary to explore greener and more environmentally friendly methods to prepare metal-free nitrogen-doped porous carbon materials with high catalytic activity toward ORR.

In this study, the MOF-derived nitrogen-doped porous carbon materials for an ORR electrocatalyst were successfully prepared. The N-containing rich ligand H_6TATAT was chosen to synthesize a MOF $[(CH_3)_2NH_2]_6[Ni(H_2O)_6]_3\{Ni_6(\eta^6\text{-TATAT})_4(H_2O)_{12}\}$ using a solvothermal reaction, which facilitated the incorporation of abundant nitrogen-containing active sites into the carbon matrix. Then, the as-synthesized MOF was directly carbonized at 800 °C, followed by modification with urea and a sintering process at 800 °C, 900 °C or 1000 °C to obtain the rich N-doped NPCs (denoted as NPC-800, NPC-900 and NPC-1000). The electrocatalytic activities of the NPCs for ORRs are carried out in an alkaline electrolyte (0.1 M KOH aqueous solution), and 20% commercial platinum/carbon is employed for the control group.

Experimental

Reagents and materials

All chemicals were reagent grade and used without further purification. H_6TATAT was synthesized according to the literature.[46]

Synthesis of the MOF

The MOF, $[(CH_3)_2NH_2]_6[Ni(H_2O)_6]_3\{Ni_6(\eta^6\text{-TATAT})_4(H_2O)_{12}\}$, was synthesized according to the previously reported literature.[46] The PXRD pattern of the as-prepared MOF consistent with the previously reported pattern of this MOF (Fig. S1†).

Preparation of NPCs

The above prepared MOF was directly carbonized at 800 °C under Ar atmosphere for 3 h in a vacuum tubular furnace at a heating rate of 4 °C min^{-1}. Then, the carbonized MOF was treated with diluted hydrochloric acid to remove probable inorganic impurities, and the resulting product was rinsed with deionized water until the filtrate had neutral pH. The collected product was vacuum dried at 60 °C for 5 h. The carbonized MOF was soaked for 12 h in a methanol solution that contained urea (the mass ratio of the carbonized MOF : urea is 1 : 3) and then carbonized at 800 °C, 900 °C and 1000 °C under ultrapure Ar for 1 h to obtain NPC-800, NPC-900 and NPC-1000.

Characterizations

Powder X-ray diffraction (PXRD) patterns were collected using a Bruker D8 Advance diffractometer at 40 kV and 40 mA using Cu-K_α radiation as the X-ray source in the 2θ range of 5–60°. Scanning electron microscopy (SEM) images were obtained with a Hitachi SU8010 system (Japan). Transmission electron microscopy (TEM) images were taken using a Hitachi JEM-2100 system (Japan). X-ray photoelectron spectroscopy (XPS) measurements were performed with an ESCALAB 250 Imaging Photoelectron Spectrometer using the monochromatic Al K_α line (1486.6 eV). Raman spectra were recorded on a Renishaw confocal spectrometer with 633 nm laser excitation. The N_2 adsorption and desorption isotherms were measured at 77 K on a Micromeritics Tristar II 3020 analyser.

Electrochemical measurements

All electrochemical experiments were conducted on a CHI 660E electrochemical station (Shanghai Chenhua Co., China) in a standard three-electrode cell at room temperature. An Ag/AgCl electrode with saturated KCl was used as the reference electrode, and a Pt wire was used as the counter electrode.

A glassy carbon electrode (GCE) of 3 mm diameter and a rotating disk electrode (RDE) of 5 mm diameter were polished mechanically with alumina slurry (Aldrich, 50 nm) to obtain a mirror-like surface and washed with deionized water and ethanol, and then allowed to dry at room temperature. To prepare the working electrodes, 5 mg of as-prepared carbon materials (carbonized MOF, NPC-800, NPC-900 or NPC-1000) were added into 1 mL absolute ethyl alcohol; then, 50 μL 5 wt% Nafion® 117 (DuPont, USA) was added into the above solution, and subsequently the solution was treated by sonication until it formed a homogeneous ink. Then, 5 μL of the suspension was drop-casted on GCE or RDE, and the modified electrode was dried at room temperature for the ORR. For comparison, a commercially available Pt/C (20 wt%, Johnson Matthey) catalyst was prepared in the same way.

Cyclic voltammetry (CV) curves were obtained in Ar- or O_2-saturated 0.1 M KOH solution at a scan rate of 50 mV s^{-1} under the potential range of −1.0 to 0.2 V and compared with the commercial Pt/C catalysts. Linear sweep voltammetry (LSV) curves were studied using a rotating disk electrode (RDE), which was measured in an O_2 saturated 0.1 M KOH solution,

and the potential was varied from 0.2 to −1.0 V with a scan rate of 10 mV s^{-1} at various rotating speeds from 400 to 2400 rpm.

Results and discussion

The synthetic route of NPC-900 is illustrated in Scheme 1. First, MOFs as precursors were carbonized at 800 °C, to obtain the porous carbon material (carbonized MOF). Second, the carbonized MOF was etched with diluted hydrochloric acid to remove probable inorganic impurities; urea as an additional nitrogen source soaked into the carbonized MOF. Finally, the mixture was heated at 800 °C, 900 °C and 1000 °C, thus forming the NPC-800, NPC-900 and NPC-1000, respectively.

The morphologies and structural features of the as-prepared NPC-800, NPC-900 and NPC-1000 are detected using SEM and TEM. The images of NPC-900 are shown in Fig. 1. The SEM and TEM image of NPC-800 and NPC-1000 are shown in Fig. S2 and S3,† respectively. It is clear that Ni nano particles (NPs) are not found in the porous carbon, as observed from Fig. 1a–c. The close view of NPC-900 further reveals that the porous carbon shows a uniform hollow sphere structure with an approximate diameter of 8.25 nm. The edge of the hollow carbon surrounded by the abundant graphitic carbon nanostructures indicates the effective catalytic graphitization by Ni NPs[47] during the sintering process. The graphitized nanostructure shows a clear lattice spacing of 0.284 nm. NPC-800 and NPC-1000 clearly show nearly the same structures. The image in Fig. 1d is the SEM image of NPC-900, which shows a complete transformation to the superficies porous carbon material.

The PXRD analysis of the porous carbons was carried out to validate their graphitic nature (Fig. 2). Two broad peaks located at approximately 25° and 44° could be assigned to the (002) and (101) planes of the carbon materials. The results confirm the presence of long-range two-dimensional ordering in the carbon matrices along with some graphitization. In addition, no diffraction peaks of impurities could be observed, which suggests the complete conversion of the carbonaceous materials after the sintering of NPCs.

The Raman spectra of NPC-800, NPC-900 and NPC-1000 are shown in Fig. 3d. Raman spectrum is a powerful tool to identify the characteristic D and G bands of the carbon materials. The D band at 1328 cm^{-1} is due to the hybridized vibrational mode associated with the edges and defects of NPCs, while the G band at 1580 cm^{-1} is attributed to tangential oscillation and vibration from all the sp^2 carbon atoms in the NPCs. Therefore, the intensity ratio of D and G bands (I_D/I_G) is often used to evaluate the defect density in carbon materials. However, these values are almost the same (approximately 1.2), which suggest that for all the synthesized porous carbons, the graphene sheets were not well developed, and the local carbon structures contained both graphene and disordered carbons. Moreover, the appearance of distinct peaks at 2680 cm^{-1} (2D band) and 2900 cm^{-1} (D + G band) in the Raman spectra further confirms the presence of highly graphitized nanostructures. This result is consistent with the TEM images.

The full XPS elemental survey scans of the surface of the NPC-900 catalyst are presented in Fig. 3a. Peaks corresponding

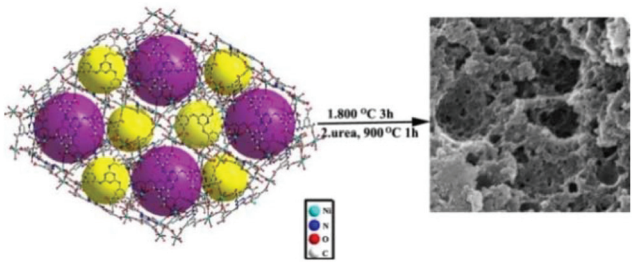

Scheme 1 Schematic of the synthetic process of the NPC-900.

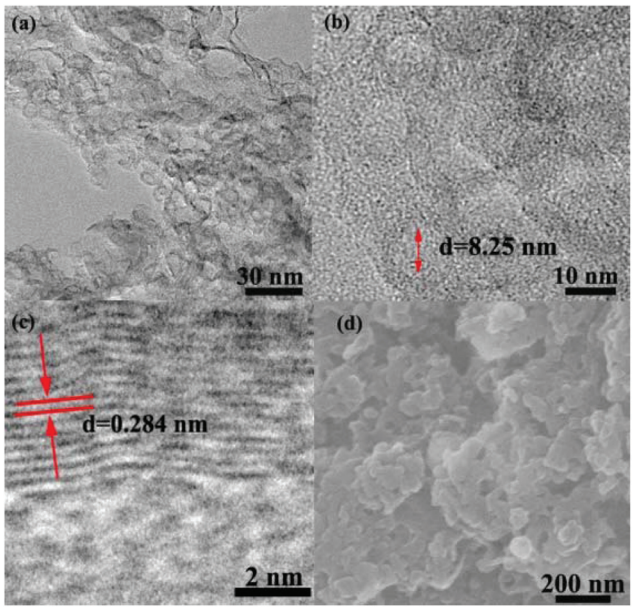

Fig. 1 TEM (a and b), HRTEM (c) and SEM (d) images of NPC-900.

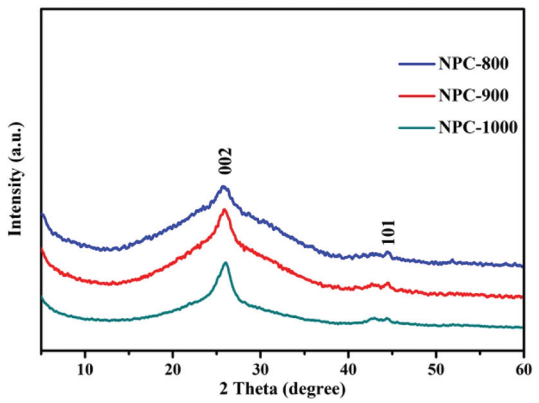

Fig. 2 The PXRD patterns of NPC-800, NPC-900 and NPC-1000.

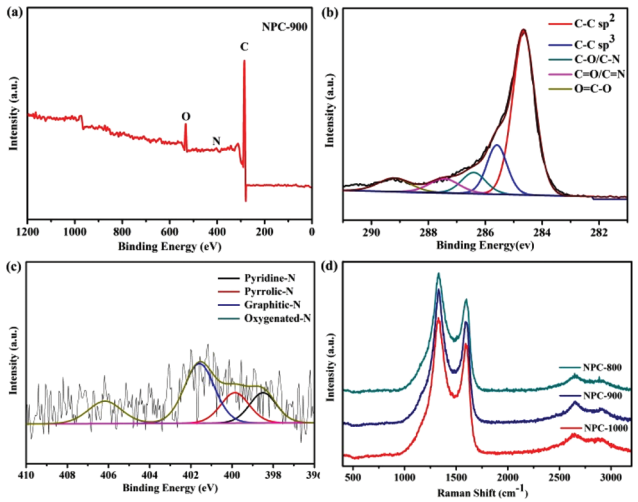

Fig. 3 Typical survey scan XPS spectrum (a), deconvoluted C 1s spectrum (b) and deconvoluted N 1s spectrum (c) of NPC-900, Raman spectra of NPC-800, NPC-900, NPC-1000 (d).

to C, N, O are clearly observed. Moreover, there are only C, N and O elements with different content observed for NPC-800 and NPC-1000 (as shown in Fig. S4 and S5†). As shown in Fig. S6,† the N atom is not detected in the carbonized MOF from the EDS analysis results. The deconvoluted C 1s signal, as shown in Fig. 3b, demonstrates a slightly asymmetric tail at higher binding energy, which is a common characteristic of nitrogen-doped carbon materials. The two main peaks at 284.6 and 285.5 eV are assigned to sp^2-hybridized graphite-like carbon (C–C sp^2) and sp^3-hybridized diamond-like carbon (C–C sp^3), respectively. The peaks centered at 286.6, 287.6 and 289.1 eV are attributed to surface oxygen and nitrogen groups (designated as C–O/C–N, C═O/C═N and O═C–O, respectively).

N actually comes from urea, which also provides evidence of successful doping. The high resolution N 1s spectrum (Fig. 3c) can be deconvoluted to four sub-peaks due to the spin–orbit coupling, including pyridinic-N (398.6 eV), pyrrolic-N (400.7 eV), graphitic-N (401.6 eV) and pyridine-*N*-oxide groups (404.5 eV). It was found that with increasing carbonization temperature from 800 °C to 1000 °C under the same 4 h carbonization time, the total N content decreased and NPC-900 showed the highest N content (1.37%) compared to NPC-800 (1.11%) and NPC-1000 (0.97%). Furthermore, there is more pyridinic-N and graphitic-N in NPC-900, which is beneficial for promoting the efficiency of ORR.

Nitrogen adsorption–desorption tests are carried out to investigate the surface area and porosity of NPC-800, NPC-900 and NPC-1000; the adsorption–desorption isotherms and the corresponding pore-size distribution curve are shown in Fig. S7–S9.†

The BET isotherm exhibits the type IV with a H3-type hysteresis loop (P/P_0 > 0.4), which indicates the mesoporous characteristics of NPC-900. Pore size is calculated using the BJH method, and the results are shown in the inset of Fig. S8.† The average pore size of NPC-900 is about 8.4 nm, which is approximately the same as that of NPC-800. The average pore size of NPC-1000 is only 7.1 nm. The BET surface areas of NPC-900, NPC-800 and NPC-1000 are 279.5 $m^2\ g^{-1}$, 258.9 $m^2\ g^{-1}$ and 249.8 $m^2\ g^{-1}$, respectively, while their cumulative pore volumes are 0.59 $cm^3\ g^{-1}$, 0.56 $cm^3\ g^{-1}$ and 0.44 $cm^3\ g^{-1}$, respectively (as shown in Fig. S7 and S9†). NPC-900 shows the largest BET surface area and cumulative pore volume. These results indicate that the high surface areas and pores of the MOFs can be well maintained after the high-temperature treatment process, which is beneficial for enhancing the transport of oxygen and the electrolyte onto the surface of the catalyst.

The performance of NPC-800, NPC-900 and NPC-1000 as electrochemical catalysts for the oxygen reduction reaction (ORR) was investigated by cyclic voltammetry (CV) and linear sweep voltammetry (LSV) on a rotating disk electrode (RDE). For the three-electrode cell, the glassy carbon (GC) electrode, Pt wire and Ag/AgCl electrodes were used as working, counter and reference electrodes, respectively. The commercial Pt/C (20 wt%) was employed as the control group. CV measurements were recorded at a scanning rate of 50 mV s^{-1} and under the potential range from −1.0 to 0.2 V (*vs.* Ag/AgCl). As shown in Fig. 4b, the carbonized MOF, NPC-800, NPC-900 and

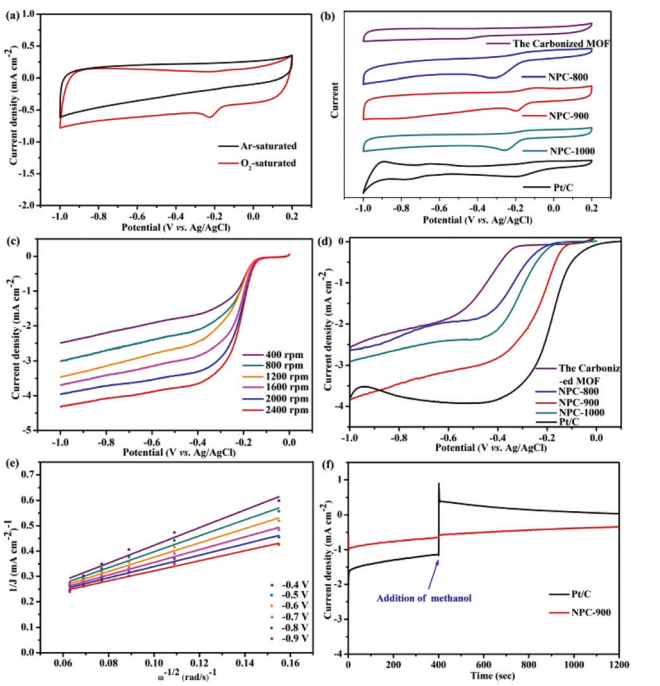

Fig. 4 (a) CV curves of the NPC-900 catalyst in O_2-saturated (rad line) or Ar-saturated (black line) 0.1 M KOH at the scan rate of 50 mV s^{-1}. (b) CV curves obtained in O_2-saturated 0.1 M KOH solution for the carbonized MOF, NPC-800, NPC-900, NPC-1000, and 20 wt% Pt/C. (c) LSV tests of the NPC-900 in O_2-saturated 0.1 M KOH with a sweep rate of 10 mV s^{-1} at the different rotation rates indicated. (d) LSV curves in O_2-saturated 0.1 M KOH solution at a scan rate of 10 mV s^{-1} and electrode-rotation speed of 1600 rpm. (e) Koutechy–Levich plots of NPC-900 at various potentials. (f) Chronoamperometric responses of NPC-900 and 20 wt% Pt/C upon addition of 3 M methanol into O_2-saturated 0.1 M KOH at −0.2 V.

NPC-1000 all displayed evident peaks in O_2-saturated KOH aqueous solution (0.1 M), and the reduction potential for the ORR shifted increasingly to more positive values. This was due to urea, which serves as an additional nitrogen source, soaking into the carbonized MOF and carbonized again to obtain the N-doped carbon materials, thereby benefitting the ORR. No peak current was observed in the Ar-saturated solution, which suggests that these carbon materials show electrocatalytic activities for ORRs. Notably, the peak potential of NPC-900 catalyst is −0.2 V, which is more positive than that of the other carbon materials. More importantly, the value is slightly negative compared with that of the commercial Pt/C catalyst (−0.17 V). Hence, these results clearly demonstrate that the NPC-900 catalyst is an outstanding catalyst for ORR.

LSV curves of NPC-900 were measured on a RDE at a scanning rate of 10 mV s^{-1} and rotating speeds of 400, 800, 1200, 1600, 2000 and 2400 rpm in O_2-saturated 0.1 M KOH solution. Control experiments were explored for NPC-800 and NPC-1000, as shown in Fig. S10b and S11b.† The current density was enhanced with increasing rotation rate from 400 to 2400 rpm due to facilitating diffusion of electrolytes. The onset potential for NPC-900 is about −0.06 V at 1600 rpm, which is more positive than that of carbonized MOF (−0.28 V), NPC-800 (−0.10 V) and NPC-1000 (−0.11 V) at the same rotation rate. The order of onset potentials is NPC-900 > NPC-800 > NPC-1000 > carbonized MOF, as shown in Fig. 4c and d. At a potential of −0.11 V, NPC-900 shows the highest current density of −3.85 mA cm^{-2}, while, under the current density of −0.1 mA cm^{-2}, NPC-900 still features the highest onset potential of −0.13 V. Therefore, according to the results of electrochemical tests, NPC-900 shows the highest catalytic activities for ORR, as shown in Table 1.

In general, ORR usually follows two types of reaction pathways: (i) direct four-electron reduction process; (ii) two-electron reduction process, which are shown as follows:[48]

(i) Direct four-electron pathway:

$$O_2(ads) + 2H_2O + 4e^- \rightarrow 4OH^-$$

(ii) Indirect (peroxide) pathway:

$$O_2(ads) + H_2O + 2e^- \rightarrow 2OH^- + HO_2^-.$$

The electron transfer number (n) was caculated according to Koutecky–Levich (K–L) equation:

$$J^{-1} = J_L^{-1} + J_k^{-1} = (B\omega^{1/2})^{-1} + J_k^{-1} \quad (1)$$

$$B = 0.62nFC_0D_0^{2/3}\nu^{-1/6} \quad (2)$$

$$J_k = nFkC_0 \quad (3)$$

where J is the measured current density, while J_k and J_L are the kinetic and diffusion-limiting current densities (mA cm^{-2}), respectively. B is Levich slope, which is given by (2). n is the electron transfer number for ORR. ω is the rotation rate ($\omega = 2\pi N$, N is the linear rotation speed in rad s^{-1}), F is the Faraday constant (F = 96 485 C mol^{-1}), ν is the kinetic viscosity of the electrolyte (ν = 0.01 cm^2 s^{-1}), C_0 is the concentration of O_2 (1.2×10^{-3} mol L^{-1}), and D_0 is the diffusion coefficient of O_2 in 0.1 M KOH (1.9×10^{-5} cm s^{-1}).

The linearity of the Koutecky–Levich plots and near parallelism of the fitting lines suggest first-order reaction kinetics toward the concentration of dissolved oxygen and similar electron transfer numbers for ORR at different potentials. The electron transfer number (n) is calculated to be ~3.6 at 0.4–0.9 V from the slopes of Koutecky–Levich plots (Fig. 4e). These results imply that the ORR catalysed by NPC-900 undergoes the direct four-electron pathway.

Furthermore, the tolerance of NPC-900 and commercial Pt/C toward methanol is determined upon addition of 3 M methanol into 0.1 M KOH electrolyte using the i–t technique. As shown in Fig. 4f, there is no significant change in the current density of NPC-900 after the addition of methanol. However, the Pt/C catalyst shows a sharp jump in the i–t curve due to the methanol oxidation reaction. In addition, long-term chronoamperometric experiments were carried out to evaluate the stability of the NPC-900 for ORR. As shown in Fig. 5, the NPC-900 exhibits superior durability compared to the Pt/C catalyst. It delivers a slight current loss with retention of more than 75% after 20 000 s. In contrast, the Pt/C catalyst suffers from a rapid current loss with only 48% retention. These

Table 1 Comparison of the ORR performance for different catalysts at a scan rate of 10 mV s^{-1} and electrode-rotation speed of 1600 rpm

Catalysts	Half-wave potential (V)	Onset potential (V)	Limiting current density (mA cm^{-2})	Electron transfer number
The carbonized MOF	−0.48	−0.28	−2.58	1.8
NPC-800	−0.37	−0.10	−2.62	2.1
NPC-900	−0.23	−0.06	−3.85	3.6
NPC-1000	−0.33	−0.11	−2.92	2.3
Pt/C	−0.19	−0.01	−4.00	3.9

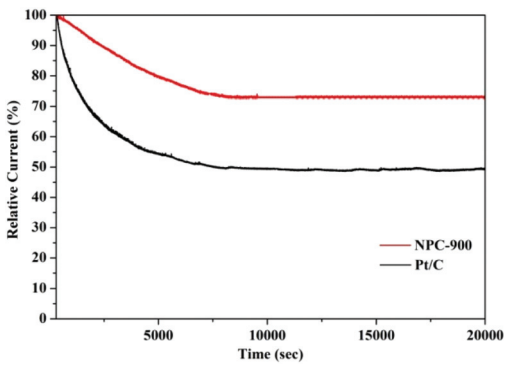

Fig. 5 Stability evaluation of Pt/C (black) and NPC-900 (red) in O_2-saturated 0.1 M KOH solution at −0.2 V and rotation speed of 1600 rpm.

results suggest that NPC-900 has much better catalytic selectivity toward the ORR than the commercial Pt/C catalyst.

Conclusions

In summary, we have developed a high performance porous N-doped carbon electrocatalyst for ORRs from $[(CH_3)_2NH_2]_6[Ni(H_2O)_6]_3\{Ni_6(\eta^6\text{-TATAT})_4(H_2O)_{12}\}$. Organic ligands from the MOF serve as a carbon source and urea as an additional nitrogen source. The Ni metal node could catalyse the graphitization of the ligand during the sintering process. NPC-900, with a high degree of graphitization, exhibits surprisingly high ORR catalytic activities in alkaline solutions, such as longer-term stability and higher methanol tolerance than the commercial Pt/C catalysts. Our findings will also provide new impetus for the development of new strategies for exploring promising non-precious-metal catalysts for energy conversion.

Acknowledgements

This study was supported by the National Natural Science Foundation of China [grant number: 21501084, 21671090, 21271096].

References

1 Y. Wang, K. S. Chen, J. Mishler, S. C. Cho and X. C. Adroher, *Appl. Energy*, 2011, **88**, 981–1007.
2 M. Nesselberger, M. Roefzaad, R. F. Hamou, P. U. Biedermann, F. F. Schweinberger, S. Kunz, K. Schloegl, G. K. H. Wiberg, S. Ashton and U. Heiz, *Nat. Mater.*, 2013, **12**, 919–924.
3 A. Anastasopoulos, J. C. Davies, L. Hannah, B. E. Hayden, C. E. Lee, C. Milhano, C. Mormiche and L. Offin, *ChemSusChem*, 2013, **6**, 1973–1982.
4 X. Yu and S. Ye, *J. Power Sources*, 2007, **172**, 145–154.
5 A. Morozan, B. Jousselme and S. Palacin, *Energy Environ. Sci.*, 2011, **4**, 1238–1254.
6 Z. Chen, D. Higgins, A. Yu, L. Zhang and J. Zhang, *Energy Environ. Sci.*, 2011, **4**, 3167–3192.
7 N. Zhang, Y. Zhang and Y. J. Xu, *Nanoscale*, 2012, **4**, 5792–5813.
8 Z. Peng and H. Yang, *Nano Res.*, 2009, **2**, 406–415.
9 R. R. Adzic, *Electrocatalysis*, 2012, **3**, 163–169.
10 B. Lim, M. Jiang, P. H. C. Camargo, E. C. Cho, J. Tao, X. Lu, Y. Zhu and Y. Xia, *Science*, 2009, **324**, 1302–1305.
11 Y. Liang, Y. Li, H. Wang and H. Dai, *J. Am. Chem. Soc.*, 2013, **135**, 2013–2036.
12 P. K. Rastogi and V. Ganesan, *Energy Environ. Focus*, 2015, **4**, 221–225.
13 P. Xu, W. Chen, Q. Wang, T. Zhu, M. Wu, J. Qiao, Z. Chen and J. Zhang, *RSC Adv.*, 2015, **5**, 6195–6206.
14 A. Morozan, S. Campidelli, A. Filoramo, B. Jousselme and S. Palacin, *Carbon*, 2011, **49**, 4839–4847.
15 J. Liu, E. Li, M. Ruan, P. Song and W. Xu, *Catalysts*, 2015, **5**, 1167–1192.
16 G. Zhang, C. Li and J. Liu, *J. Mater. Chem. A*, 2014, **2**, 8184–8189.
17 Y. Shao, J. Sui, G. Yin and Y. Gao, *Appl. Catal., B*, 2008, **79**, 89–99.
18 S. Wang, A. Roy, Y. Xue, D. Yu and L. Dai, *Angew. Chem., Int. Ed.*, 2011, **50**, 11756–11760.
19 Y. Zhao, L. Yang, S. Chen, X. Wang, Y. Ma, Q. Wu, Y. Jiang, W. Qian and Z. Hu, *J. Am. Chem. Soc.*, 2013, **135**, 1201–1204.
20 H. Tang, S. Cai, S. Xie, Z. Wang, Y. Tong, M. Pan and X. Lu, *Adv. Sci.*, 2016, **3**, 1500265.
21 M. Thomas, R. Illathvalappil, S. Kurungot, B. N. Nair, A. A. Mohamed, G. M. Anilkumar, T. Yamaguchi and U. S. Hareesh, *ACS Appl. Mater. Interfaces*, 2016, **8**, 29373–29382.
22 L. Zhang, Z. Su, F. Jiang, L. Yang, J. Qian, Y. Zhou, W. Li and M. Hong, *Nanoscale*, 2014, **6**, 6590–6602.
23 G. Wang, K. Jiang, M. Xu, C. Min, B. Ma and X. Yang, *J. Power Sources*, 2014, **266**, 222–225.
24 J. S. Li, S. L. Li, Y. J. Tang, K. Li, L. Zhou, N. Kong, Y. Q. Lan, J. C. Bao and Z. H. Dai, *Sci. Rep.*, 2014, **4**, 5130.
25 Z. W. Liu, F. Peng, H. J. Wang, H. Yu, W. X. Zheng and J. Yang, *Angew. Chem., Int. Ed.*, 2011, **50**, 3257–3261.
26 D. S. Yang, D. Bhattacharjya, S. Inamdar, J. Park and J. S. Yu, *J. Am. Chem. Soc.*, 2012, **134**, 16127–16130.
27 Y. Su, Y. Zhang, X. Zhuang, S. Li, D. Wu, F. Zhang and X. Feng, *Carbon*, 2013, **62**, 296–301.
28 Z. Yang, Z. Yao, G. Li, G. Fang, H. Nie, Z. Liu, X. Zhou, X. Chen and S. Huang, *ACS Nano*, 2012, **6**, 205–211.
29 J. Liang, Y. Jiao, M. Jaroniec and S. Z. Qiao, *Angew. Chem., Int. Ed.*, 2012, **51**, 11496–11500.
30 Z. Liu, G. Zhang, Z. Lu, X. Jin, Z. Chang and X. Sun, *Nano Res.*, 2013, **6**, 293–301.
31 C. Huang, C. Li and G. Shi, *Energy Environ. Sci.*, 2012, **5**, 8848–8868.
32 H. X. Zhong, J. Wang, Y. W. Zhang, W. L. Xu, W. Xing, D. Xu, Y. F. Zhang and X. B. Zhang, *Angew. Chem., Int. Ed.*, 2014, **53**, 14235–14239.
33 L. Ge, Y. Yang, L. Wang, W. Zhou, R. De Marco, Z. Chen, J. Zou and Z. Zhu, *Carbon*, 2015, **82**, 417–424.
34 P. Pachfule, V. M. Dhavale, S. Kandambeth, S. Kurungot and R. Banerjee, *Chem. – Eur. J.*, 2013, **19**, 974–980.
35 J. Li, Y. Chen, Y. Tang, S. Li, H. Dong, K. Li, M. Han, Y.-Q. Lan, J. Bao and Z. Dai, *J. Mater. Chem. A*, 2014, **2**, 6316.
36 C. Hu, Y. Xiao, Y. Zhao, N. Chen, Z. Zhang, M. Cao and L. Qu, *Nanoscale*, 2013, **5**, 2726–2733.
37 C. W. Tan, K. H. Tan, Y. T. Ong, A. R. Mohamed, S. H. S. Zein and S. H. Tan, *Environ. Chem. Lett.*, 2012, **10**, 265–273.
38 Y. Zhao, Z. Bakenova, Y. Zhang, H. Peng, H. Xie and Z. Bakenov, *Ionics*, 2015, **21**, 1925–1930.
39 S. Pandiaraj, H. B. Aiyappa, R. Banerjee and S. Kurungot, *Chem. Commun.*, 2014, **50**, 3363–3366.

40 Y. Z. Chen, C. Wang, Z. Y. Wu, Y. Xiong, Q. Xu, S. H. Yu and H. L. Jiang, *Adv. Mater.*, 2015, **27**, 5010–5016.
41 P. Zhang, F. Sun, Z. Xiang, Z. Shen, J. Yun and D. Cao, *Energy Environ. Sci.*, 2014, **7**, 442–450.
42 M. Jiang, X. Cao, D. Zhu, Y. Duan and J. Zhang, *Electrochim. Acta*, 2016, **196**, 699–707.
43 L. Jiao, Y. X. Zhou and H. L. Jiang, *Chem. Sci.*, 2016, **7**, 1690–1695.
44 M. Jahan, Q. Bao and K. P. Loh, *J. Am. Chem. Soc.*, 2012, **134**, 6707–6713.
45 C. Li, C. Hu, Y. Zhao, L. Song, J. Zhang, R. Huang and L. Qu, *Carbon*, 2014, **78**, 231–242.
46 Z. Zhu, Y. L. Bai, L. Zhang, D. Sun, J. Fang and S. Zhu, *Chem. Commun.*, 2014, **50**, 14674–14677.
47 M. Sevilla and A. B. Fuertes, *Carbon*, 2006, **44**, 468–474.
48 G. Zhang, C. Li, J. Liu, L. Zhou, R. Liu, X. Han, H. Huang, H. Hu, Y. Liu and Z. Kang, *J. Mater. Chem. A*, 2014, **2**, 8184.